Prediction models to analyse the performance of a commercial-scale membrane distillation unit for desalting brines from RO plants

Juan D. Gil[a], Alba Ruiz-Aguirre[a], Lidia Roca[b], Guillermo Zaragoza[b,*], Manuel Berenguel[a]

[a] *Centro Mixto CIESOL, ceiA3, Universidad de Almería. Ctra. Sacramento s/n, Almería 04120, Spain; {juandiego.gil,ara399,beren}@ual.es*
[b] *CIEMAT-Plataforma Solar de Almería, Ctra. de Senés s/n, Tabernas 04200, Almería, Spain; {lidia.roca,guillermo.zaragoza}@psa.es*

Abstract

Desalting brines from Reverse Osmosis (RO) plants is one of the most promising applications of Membrane Distillation (MD) systems. The development of accurate models to predict MD system performances plays a significant role in the design of this kind of industrial applications. In this paper, a commercial-scale Permeate Gap Membrane Distillation (PGMD) module was modeled by means of two different approaches: Response Surface Methodology (RSM) and Artificial Neural Networks (ANN). Condenser inlet temperature, evaporator inlet temperature, feed flow rate and feed water salt concentration were selected as inputs of the model, while permeate flux and Specific Thermal Energy Consumption (STEC) were chosen as responses. The prediction abilities of both RSM and ANN models were compared with further experimental data by using the Analysis of Variance (ANOVA) and the Root Mean Squared Error (RMSE). The results show that the ANN model is able to predict in a more precise way the behaviour of the module for the whole range of input variables. Thus, ANN model was used to find the optimal operating conditions, for the module operating at feed water salinity of 70 and 105 g/L, concentrations that can be reached when desalting RO brines.

Keywords: Permeate-gap Membrane Distillation, Response Surface Methodology, Artificial Neural Network, Multiobjective Optimization, Brine Treatment.

1. Introduction

Due to the high tolerance of MD systems to high salinity feeds, one of the possible industrial applications of this technology consists on desalting seawater

*Corresponding author.
Email address: guillermo.zaragoza@psa.es (Guillermo Zaragoza)

RO brines. Integrating MD technology in RO plants could be an essential factor to obtain efficient desalination lines in terms of recovery [1–4]. However, the uncertainty associated with the performance of MD technology at large scale has prevented the development of this kind of applications so far [5–8]. Therefore, investigating the performance of large scale MD systems, under the operating conditions imposed by RO brine, is required for assessing the energy efficiency which is one of the main barriers of the MD technology [6]. In this context, the development of accurate theoretical (first principles-based) or empirical models, to predict the performance of MD processes is fundamental. Models not only allow designers to simulate and analyze MD systems under the required operating conditions [9–12], but can also be used for developing real time optimization strategies [13, 14], or to develop optimization algorithms aimed at obtaining optimal designs of the application at hand [15].

The construction of first principles based models requires a total knowledge of the process to be modeled, and it is usually a laborious task. On the contrary, this knowledge is not as necessary to elaborate empirical models, but in this case a good selection of the dependent and independent variables, and a good design of experiments are needed. Additionally, in the case of MD systems, the difficulty in constructing theoretical models is greater as the different internal design of each module influences its performance. So, internal modifications of this theoretical models have to be done to adapt them to the different module designs, which in many case is non-disclosed information. For that reason, the use of empirical models is a good option to obtain a mathematical expression in a relatively fast and simple way. Two of the most common empirical models used in the field of membrane sciences to visualize the operational space and to understand the system behaviour are RSM and ANN [16, 17]. These models, also known as *black blox* models, are able to fit both linear and nonlinear multivariable problems. It should be remarked that these kind of empirical models cannot been used to extrapolate the results to other systems, and they are only valid for the range of operation in which they have been calculated.

RSM is a statistical method extensively used for characterizing membrane distillation systems. This methodology is an efficient modeling tool providing quadratic functions to fit responses in linear or smooth nonlinear processes. As can be seen in Tab. 1, most works presented until now in the literature use RSM in order to optimize MD systems in terms of two of the most important parameters in this technology: permeate production and thermal energy efficiency. However, not all works treat these two parameters in a simultaneous way [9, 18–24]. In addition, in most papers the feed water salt concentration, one of the most important paremeters influencing the performance of MD systems, is not taken into account as an input of the model [9, 12, 18, 19, 22, 23, 25, 26].

ANN is an emerging modeling tool in the field of MD systems. The main advantage of this methodology is that it is able to fit almost all nonlinear processes. Besides, the way in which the model is built allows retraining the model with further experimental data for improving predictions. Tab. 2 summarizes the proposals made up to now in the literature for modeling MD systems by means of ANN based models. As can be seen, almost all the works use ANN for characterizing only the permeate production of a MD unit [10, 11, 14, 27, 28], and only Shibazian and Alibabaei [29] consider also the thermal energy. Furthermore, the feed water salt concentration is only considered by Cao et al. [27] and Tavakolmoghadam and Safavi [28].

The goal of this work is to develop empirical models able to predict, in a precise way, the performance of a commercial-scale PGMD module for desalting RO brines. For this purpose, three main objectives are developed: i) obtaining empirical forecasting models based on RSM and ANN, under the required operating conditions, ii) comparing the prediction abilities of the two modeling approaches, and iii) finding the optimal operating conditions of this module for two of the salinity concentrations that can be reached when desalting RO brines, 70 and 105 g/L. Compared to most modeling approaches presented until now in the literature (see Tabs. 1 and 2), in this work, both the permeate production and the thermal energy consumption were selected as predicted performance parameters. In addition, apart from the typical independent variables considered in this technology (condenser inlet temperature, evaporator inlet temperature, and feed flow rate), the feed water salt concentration (35-140 g/L) has been used as an input, in order to visualize the effect of this parameter in the responses. It should be pointed out that most of the studies presented in the literature use bench-scale modules, whereas this study has been performed using a commercial-scale module, which can be very relevant to commercial purposes.

Reference	MD configuration	Inputs and ranges	Outputs
[30]	VMD	Feed inlet temperature (30-70 °C) NaCl concentration in feed solution (1-9 %) Feed velocity (1-17 m/min) Module packing density (5-45 %) Length-diameter ratio of module (3.3-16.7)	Water permeate flux (kg/(h·m^2)) Water productivity per unit volume of module (kg/(h·m^3)) Gained Output Ratio (GOR) Comprehensive index
[31]	-	Feed solution (0.4-0.9 L/min) Flow rate draw solution (0.3-0.7 L/min) Feed solution salt concentration (3-5 M)	Permeate salt concentration (g/L)
[12]	PGMD	Feed flow rate (400-600 L/h) Condenser inlet temperature (20-30 °C) Evaporator inlet temperature (60-80 °C)	Permeate flux (L/(h·m^2)) STEC (kWh/m^3)
[32]	AGMD	Hot feed inlet temperature (40-80 °C) Cold feed inlet temperature (10-50 °C) Feed conductivity (500-10000 μS/cm) Feed flow rate (4-8 L/min)	Permeate flux (kg/(h·m^2)) Specific performance ratio
[18]	AGMD	Feed flow rate (1-5 L/min) Feed temperature (60-80 °C) Coolant temperature (60-80 °C) Coolant flow rate (1-3 L/min) Air gap width (3-7 mm)	Permeate flux (L/(h·m^2))
[19]	DCMD	Feed temperature (46.6-63.4 °C) Permeate temperature (6.6-23.4 °C) Feed flow rate (199-451 L/h) Permeate flow rate (199-451 L/h)	Permeate flux (kg/(h·m^2))

The table continues in the next page

Reference	MD configuration	Inputs and ranges	Outputs
[25]	DCMD	Feed inlet temperature (40-80 °C) Permeate inlet temperature (15-35 °C) Flow velocity of feed solution (6-54 m/min) Module packing density (5-45 %) Length-diameter ratio of module (2.9-8.35)	Average permeate flux (kg/(h·m^2)) Production per unit volume of module (kg/(h·m^3)) Production per unit energy consumption (kg/kJ) Comprehensive index
[20]	VMD	Feed temperature (25-55 °C) Vacuum pressure (10-90 mbar) Feed flow rate (15-60 mL/s) Feed concentration (100-300 g/L)	Permeate flux (kg/(h·m^2))
[26]	AGMD	Cold feed inlet temperature (23.2-56.8 °C) Hot feed inlet temperature (58.5-91.8 °C) Feed inlet flow rate (23.7-84.3 L/h)	Permeate flux (L/(h·m^2)) GOR
[21]	DCMD	Vapor pressure difference(3.5-35.5 10^3Pa) Permeate flow rate (5.2-28.8 L/h) Feed flow rate (6.4-73.6 L/h) Feed ionic strength (21.4-338 mM)	Permeate flux (L/(h·m^2))
[22]	AGMD	Cooling inlet temperature(13.9-26.1 °C) Feed inlet temperature(59-71 °C) Feed flow rate (145-205 L/h)	Specific performance index (kg/kWh)
[9]	SGMD	Water inlet temperature (58-72 °C) Air inlet temperature (17.2-22.8 °C) Water circulation velocity (0.16-0.25 m/s) Air circulation velocity (1.03-2.13 m/s)	Permeate flux (kg/(s·m^2))

The table continues in the next page

Reference	MD configuration	Inputs and ranges	Outputs
[23]	DCMD	Hot fluid flow rate (1-4 10^{-2}kg/s) Hot fluid temperature (45.2-84.74 °C) Cold fluid flow rate (1.5-4 10^{-2}m^3/s) Membrane thickness (30-150 μm)	Recovery ratio (%)
[23]	AGMD	Hot fluid flow rate (1.72-4.17 10^{-2}kg/s) Hot fluid temperature (45-75 °C)	Recovery ratio (%)
[24]	DCMD	Stirring velocity (88.2-786.8 rpm) Feed temperature (22.3-52.7 °C) NaCl concentration (0.007-2.193 M)	Permeate flux (m/s)

Table 1: Existing RSM modeling approaches in MD systems. AGMD is the Air-Gap membrane Distillation configuration, DCMD is the Direct Contact Membrane Distillation configuration, VMD is the Vacuum Membrane Distillation one, and SGMD is the Sweeping Gas Membrane Distillation configuration.

Reference	MD configuration	Inputs and ranges	Outputs	Topology
[29]	AGMD	Cold inlet temperature (23.2-56.8 °C) Hot feed inlet temperature (65-91.8 °C) Feed-in flow rate (36-84.3 L/h)	Permeate flux (L/(h·m^2)) Cold outlet temperature (°C) GOR	-
[27]	VMD	Feed inlet temperature (60-70.44 °C) Vacuum pressure (0.037-0.089 MPa) Feed flow rate (69.89-111 L/h) Feed water salt concentration (30-45 g/kg)	Permeate flux (kg/(s·m^2))	4:3:1
[14]	PGMD	Feed flow rate (L/h) Cold inlet temperature (°C) Irradiance (W/m^2)	Permeate flow rate (L/h)	3:5:1
[11]	SGMD	Feed inlet temperature (54-68 °C) Air flow rate (0.966-2.028 m/s) Feed flow rate (0.140-0.206 m/s)	Permeate flux (kg/(s·m^2))	3:9:1
[10]	AGMD	Air gap thickness (3.0-7.4 mm) Cold inlet temperature (13.9-26.1 °C) Feed inlet temperature (30-71 °C) Feed flow rate (145-205 L/h)	Permeate flux (kg/(s·m^2))	4:10:1
[28]	VMD	Vacuum pressure (10-80 mbar) Feed temperature (25-55 °C) Salt concentration (50-300 g/L) Feed flow rate (15-60 mL/s)	Permeate flux (kg/(s·m^2))	4:3:1

Table 2: Existing ANN modeling approaches in MD systems. All the approaches used Multi-Layer feedforward Perceptron Networks.

2. Methodology

2.1. Test-bed facility

In this study, a spiral wound MD commercial module called Oryx 150 was evaluated (see Fig. 1-b). The module was designed by the Fraunhofer Institute for Solar Energy systems and is marketed by the company Solar Spring (Freiburg, Germany). It had a Permeate Gap Membrane Distillation (PGMD) configuration. The location of the different channels of the module was placed to minimize heat losses to the environment. All inlets and outlets were located at the top of the module. The permeate outlet was located on the outer perimeter of the coil to facilitate the recovery of sensible heat from the permeate. This module had a length, a height and a channel width of 7 m, 0.7 m and 3.2 mm respectively. The membrane surface area was 10 m^2. The membrane used in the module was a commercial membrane of W. L. Gore Associates. The membrane was constituted by an active Polytetrafluoroethylene (PTFE) layer with a nominal pore size of 0.2 μm, a thickness of 70 μm and a porosity of 80 % and a support of Polypropylene (PP) with a thickness of 280 μm and a porosity of 50 %. The spacers were made of Low-Density Polyethylene (LDPE) and the condensation foil was made of Ethylene Tetrafluoroethylene (ETFE). The permeate gap was created by a PP spacer of 1 mm. The Oryx 150 module was integrated into a structure that was formed by a feed tank (475 L), a filter of 300 μm placed after the outlet of the feed tank and before the inlet of the MD module, the pump to circulate the feed solution, a deaerator and the heat exchanger. Four PT100 temperature sensors were placed directly at the inlet of the evaporator and condensation channels and at the outlets of them (see Fig. 2). The fifth temperature sensor was located at the inlet of the heat exchanger on the side of the heating fluid (see Fig. 2). The volumetric flow rate (F in Fig. 2) was measured with a flow meter placed before the inlet of the condenser channel. A pressure sensor (WIKA) was located at the inlet of the condenser channel to avoid overpressure. The permeate was measured with a weight (W in Fig. 2), using a tank to collect the permeate, and then, returning it to the feed tank. All the temperature and pressure measurements were monitored and registered by a Supervisory Control And Data Acquisition (SCADA) system connected through a Programmable Logic Controller (PLC).

The MD module was tested in the Solar Membrane Distillation (SMD) pilot facility of Plataforma Solar de Almería (PSA, www.psa.es) (see Fig. 1-a). In this facility, the module was connected to a solar field through a heat exchanger. The solar field was formed by 10 flat plate collector (Solaris CP1 Nova, Solaris, Spain) divided into two files with 5 collectors each one. The nominal thermal power supplied was 7 kW_{th} at a temperature of 90 °C. The heat rate supplied to the heat exchanger was controlled by means of the feedback control structure presented in [33].

The operation of the MD system consisted of pumping the cold feed solution to the condenser inlet. The low temperature of the feed solution helped the condensation of the permeate. The circulation of the feed solution along the condensation channel allowed preheating the solution thanks to the latent

(a) SMD facility. (b) Solar Spring pilot module.

Figure 1: Test-bed facility at Plataforma Solar de Almería (PSA).

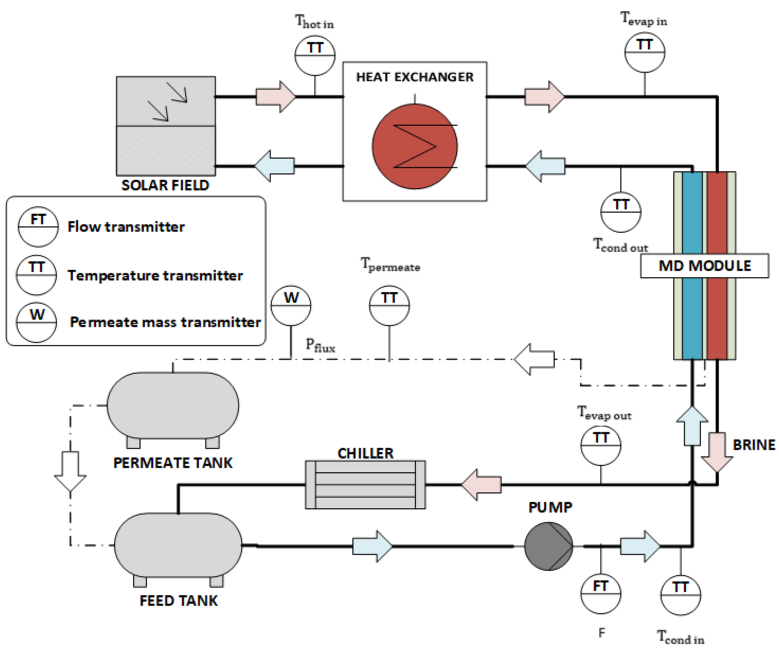

Figure 2: Schematic diagram of the test-bed facility.

heat of condensation and to the sensible heat that crossed the membrane. After leaving the condensation channel, the solution passed to the deaerator to eliminate the non-condensable gases from the feed solution and later it was circulated towards the inlet of the heat exchanger. Afterwards, the hot feed went into the evaporator channel and circulated countercurrent with respect to the circulation in the condensation channel. As the feed circulated along the evaporator channel, the vapour passed through the pores of the membrane driven by the vapour pressure difference created on both sides of the membrane due to the temperature difference. The concentrated feed solution (brine) left the module through the outlet of the evaporator channel and was poured into the feed tank for recirculation. Since the brine had a temperature above that of the feed solution, it was cooled down with a chiller.

2.2. Thermal energy performance metric

The thermal efficiency of the distillation process can be evaluated by means of several metrics, being the Specific Thermal Energy Consumption (STEC), the one adopted in this work, one of the most employed [12, 34–36]. This metric provides the thermal energy required per volume unit of distillate, and it can be calculated as follows:

$$\mathrm{STEC}\ (\mathrm{kWh/m^3}) = \frac{\mathrm{F} \cdot \rho_{feed} \cdot c_p \cdot (\mathrm{T_{evap\,in}} - \mathrm{T_{cond\,out}})}{c \cdot \mathrm{D}}, \tag{1}$$

where c is a conversion factor ($3.6{\cdot}10^6$ s·W/(h·kW)), ρ_{feed} is the feed water density (kg/m^3), c_p is the heat water capacity (J/(kg·^{o}C)), D is the permeate flow rate (L/h), and the rest of variables are according to Fig. 2.

2.3. Response Surface Methodology (RSM)

RSM is a set of mathematical and statistical techniques based on the fitting of empirical models to the experimental data obtained through an experimental design. The RSM procedure consists of the development of a linear or quadratic polynomial function that adjusts the response (permeate production, energy efficiency and so on) depending on the operating conditions (temperatures, flow rates and so on). Therefore, polynomial functions are used to describe the studied system and consequently, to explore (model and displace) the experimental conditions up to their optimization to achieve the best performance of the system [37].

The development of a RSM has several steps: (i) selection of the main variables that exert the highest effect on the system through the screening studies and the delimitation of the experimental region, in accordance with the goal of the study and the experience of the researcher; (ii) choice of an experimental design that defines which experiments should be carried out in the experimental region and conduction of the experiments according to the selected experimental matrix; (iii) mathematical-statistical treatment of the experimental data by adjusting a polynomial function (see Eq. 2); (iv) evaluation of the validity of the model.

$$y = \beta_0 + \sum_{i=1}^{k} \beta_i \cdot x_i + \sum_{i=1}^{k} \beta_{ii} \cdot x_i^2 + \sum_{1 \le i \le j}^{k} \beta_{ij} \cdot x_i \cdot x_j, \tag{2}$$

where k is the number of variables, β_0 is the offset term coefficient, β_i represents the coefficients of the linear effects, x_i and x_j represents the variables, β_{ij} represents the coefficients of the interaction of effects, and β_{ii} represents the coefficients of the quadratic parameters. To estimate the coefficients of the equation, the experimental design must ensure that all the studied variables are carried out for at least three levels of each variable. Among the most used second order design are the three-level factorial design, the Box-Behnken design and the central composite design. These designs differ from each other in their selection of experimental points, number of levels for the variables and number of executions. In particular, central composite design is a fractional factorial or factorial design with extended central points with a group of axial points also called star points. So, for example, to optimize a process with three variables ($k = 3$), the first block is a factorial 2^3, the second block is a set of 2x3 tests and the third blocks are repetitions in the center [38]. There are three types of central composite design, specifically, circumscribed, inscribed and face-centered central composite. In the last one, the star points are the center of each face of the vector space, so this variety requires only three levels of for each factor. After the experimental plan proposed by the design has been carried out and the values of the responses have been obtained for each experimental point, it is necessary to evaluate the quality of the adjusted model by applying the ANOVA [39]. With the ANOVA, the variation due to the treatment (change in the combination of the levels of the variables) is compared with the variation due to the random errors inherent in the measurements of the generated responses. From this comparison, it is possible to evaluate the significance of the regression used to predict the answer.

2.4. Artificial Neural Network (ANN)

An ANN is also a mathematical model which is composed by simple interconnected elements, that process information in response to external inputs, trying to imitate the behaviour of biological neural networks. These simple elements, called neurons, are computational processors in which three main operations (see Fig. 3) are carried out [40, 41]:

1. The n-element input vector (z_1, z_2, ...z_n) is multiplied by weights ($\mathrm{w}_{1,1}$, $\mathrm{w}_{1,2}$, ...$\mathrm{w}_{1,n}$).
2. In the summing junction, the weighted inputs are added together with the bias vector b, obtaining the argument a:

$$a = \mathrm{z}_1 \cdot \mathrm{w}_{1,1} + \mathrm{z}_2 \cdot \mathrm{w}_{1,2} + ... + \mathrm{z}_n \cdot \mathrm{w}_{1,n} + b. \tag{3}$$

3. Finally, the argument a is converted into a scalar value Out by means of the transfer function f (see Fig. 3):

$$Out = f(\mathbf{zW} + b). \tag{4}$$

In the transfer function block (f in Fig. 3), several functions can be employed, being the linear (*purelin*) and the log-sigmoid (*logsig*) transfer functions two of the most adopted [40, 41]. Thus, the outputs of neurons calculated by these transfer functions can be expressed as:

$$\text{Purelin} : Out = f(a) = a, \tag{5}$$

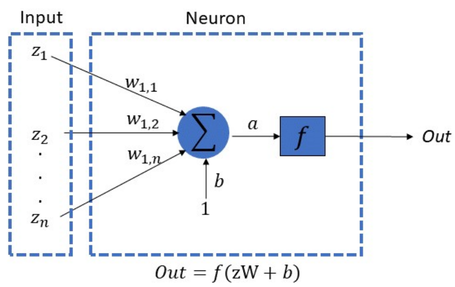

Figure 3: Schematic diagram of an artificial neuron.

$$\text{Logsig} : Out = f(a) = \frac{1}{1 + e^{a}}. \tag{6}$$

The form in which neurons are grouped and connected is known as topology or architecture of the neural network. In general, neurons are grouped in different layers such as hidden and output layers. Moreover, the inputs can be treated as an additional layer. Between the different kinds of architectures, one of the most used to perform function fitting is the Multi-Layer feedforward Perceptron (MLP) [42]. In this architecture, the number of inputs and outputs of the network is defined according to the number of input and output variables of the system to be modeled. On the other hand, the optimal selection of the number of layers, and the number of neurons required in each layer, is still an active research area and it is usually obtained by trial and error. In practice, most neural networks have only two or three hidden layers [42].

Once the architecture of the network is chosen, the weights and biases are adjusted by mean of a training algorithm. Back Propagation (BP) algorithm is the most commonly employed for training MLP networks [10, 11, 17, 42]. This algorithm tries to minimize a performance function by iteratively adjusting network weights and biases. The index used as performance function in this work is the Root Mean Square Error (RMSE):

$$\text{RMSE} = \sqrt{\frac{\sum_{i=1}^{M} \sum_{j=1}^{N} (Y_{i,j} - \hat{Y}_{i,j})^2}{M \cdot N}}, \tag{7}$$

where M is the number of network outputs, N is the number of data used for training, and $Y_{i,j}$ and $\hat{Y}_{i,j}$ is the experimental and predicted response respectively. Thus, in each iteration BP algorithm modifies weights and biases in the direction in which RMSE decreases. One iteration of this algorithm is given by [42]:

$$\boldsymbol{\lambda}_{k+1} = \boldsymbol{\lambda}_k - \delta \boldsymbol{\Delta}_k, \tag{8}$$

where $\boldsymbol{\lambda}_k$ is a vector containing current network weights and biases, δ is the learning rate, $\boldsymbol{\Delta}_k$ is the current gradient of RMSE function, and k being the iteration number.

2.5. Multi-objective optimization

The space of solutions of the RSM model can be easily explored by a conventional gradient-based optimization method, as it is quadratic. However, the ANN model does not guarantee a linear or smooth nonlinear solution space to be explored. Therefore, other global techniques such as genetic-based algorithms should be considered. In this work, a multi-objective evolutionary algorithm NSGA-II was employed to carry out the optimization. NSGA-II is a fast and elitist optimizing approach which stands out for obtaining spread solutions near the optimal Pareto Front. In general, the algorithm can be roughly divided in the following steps:

1. Creation of an initial population randomly selected according to the problem and constraints.
2. Nondominated sorting of the population inizializated previously.
3. Calculation of the crowding-distance.
4. Selection of individuals based on a crowded-comparison operator.
5. Use crossover and mutation operators to generate a new population.

All the steps are widely explained in [43]. The optimization was carried out with Matlab R2018a (the Mathworks, USA). The population size of the algorithm was fixed at 10, the maximum number of iterations at 500, and the convergence tolerance was 1e-100.

3. Results and discussion

Variable	Nomenclature	Range
Evaporator inlet temperature (°C)	T_{evap}	60-80
Condenser inlet temperature (°C)	T_{cond}	20-30
Feed flow rate (L/h)	F	400-600
Feed water salt concentration (g/L)	S	35-140

Table 3: Input model variables.

3.1. Response Surface Methodology based model

RSM was used to characterize the performance of MD module through the specific thermal energy consumption (STEC) and permeate flux (P_{flux}), as a function of the main parameters that affect the performance in this technology, which are summarized in Tab. 3. Notice that the variables have been selected according to the allowed operational limits of the module [12], since the objective is to perform a realistic study in commercial-scale. After choosing the variables, , the Design of the Experiment (DoE) was carried out with Statgraphics centurion, a highly specific multivariate analysis package. The chosen design to obtain the experimental campaign was the Face-centered Central Composite (CCF) design which required three levels of each of the variables. The data proposed by the CCF design for modeling are presented in Appendix A.

Terms	P_{flux}(L/(h·m^2))		STEC(kWh/m^3)	
	Coefficient	P-value	Coefficient	P-value
T_{evap}	0.039820	0.0000	-75.525	0.0006
T_{cond}	-0.000171	0.0000	105.672	0.0505
F	0.002683	0.0000	-6.079	0.1223
S	-0.010709	0.0000	26.804	0.0000
${T_{evap}}^2$	-0.000065	0.7800	0.613	0.5504
$T_{evap}·T_{cond}$	-0.000063	0.7383	-1.365	0.1147
T_{evap}·F	0.000062	0.0000	0.059	0.1651
T_{evap}·S	-0.000208	0.0000	-0.273	0.0042
${T_{cond}}^2$	-0.000181	0.8463	0.613	0.8804
T_{cond}·F	0.000006	0.7383	-0.113	0.1838
T_{cond}·S	-0.000107	0.0104	0.368	0.0336
F^2	-0.000004	0.1374	0.005	0.5966
F·S	-0.000009	0.0002	-0.014	0.0758
S^2	0.000132	0.0000	-0.024	0.5127

Table 4: Values of the regression coefficients and their statistical significance.

After carrying out the experimental campaign and introducing the experimental values of the responses of interest, the experimental design was analyzed. The ANOVA analysis was used to verify if the regression equations were statistically valid. The statistical parameters used to evaluate the goodness of the fit was the p-value, the coefficient of determination (R^2) and the adjusted coefficient of determination (adjusted-R^2). Specifically, the p-value was used to determine which terms of the equation were statistically significant. For that, the p-value was compared with the level of significance to decide which terms were excluded from the final model. A value of 0.05 was used for the level of significance, meaning that if the p-value was lower than 0.05, the coefficient was significantly different from zero with a confidence level of 95 %. Therefore, the coefficients with a p-value higher than 0.05 were not included in the final equations. Tab. 4 shows the p-values of the coefficients for both responses (STEC and P_{flux}). Thus T_{evap}, T_{cond}, F, S, T_{evap}·F , T_{evap}·S , T_{cond}·S, F·S and S^2 were significant for Pflux while for STEC, only T_{evap}, S and T_{evap}·S were statistically significant. Non-significant terms were removed from the model to obtain the simplified equations for both Pflux and STEC:

$$\begin{aligned} P_{flux} = &-0.8868 + 0.0291 \cdot T_{evap} - 0.0104 \cdot T_{cond} - 0.0008 \cdot F - 0.0087 \cdot S \\ &+ 0.000061 \cdot T_{evap} \cdot F - 0.0002 \cdot T_{evap} \cdot S - 0.0001 \cdot T_{cond} \cdot S \\ &- 0.000009 \cdot F \cdot S + 0.0001 \cdot S^2 \end{aligned} \tag{9}$$

$$STEC = -317.712 + 5.874 \cdot T_{evap} + 24.296 \cdot S - 0.273 \cdot T_{evap} \cdot S \tag{10}$$

The simplified equations were also subjected to an analysis of variance. Tab. 5 shows the values of the statistics for the simplified models for P_{flux} and

STEC. The p-value and the coefficients of determination determined a good fit for Pflux but the R^2 and adjusted-R^2 were low for the STEC. The comparison between the observed values and the adjusted values by the models is shown in Fig. 4. An excellent fit can be observed between the experimental and predicted responses for P_{flux} (see Fig. 4-1). On the other hand, the adjustment in the STEC response is not so good (see Fig. 4-2), as expected in view of the results of the ANOVA. Notice that the RSM model is composed by linear, interaction and quadratic terms, which are good at adjusting linear or quadratic behaviours, however it provides unsuccessful fitting when it comes to nonlinear behaviour, as the one obtained by the feed water salt concentration influence on the STEC. When the feed water salt concentration is not taken into account as an input of the model, RSM provides satisfactory adjustments [12].

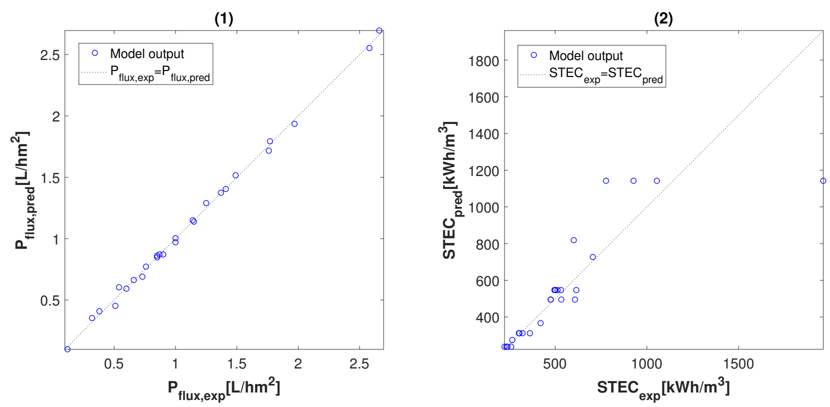

Figure 4: Comparison between predicted values by RSM model ($STEC_{pred}$ and $P_{flux,pred}$) and experimental data ($STEC_{exp}$ and $P_{flux,exp}$).

Statistical estimator	Condition for a good fit	P_{flux}	STEC
p-value	$\leq$0.05	$\leq$0.01	$\leq$0.02
R^2	closed to 1	0.998	0.704
adjusted-R^2	in agreement with R^2	0.996	0.664

Table 5: Goodness of the adjustment of the simplified models of P_{flux} and STEC

3.2. Neural Network based model

The neural network based model was developed considering as inputs S, T_{cond}, T_{evap} and F (see Tab, 3), and as outputs P_{flux} and STEC. In this case, the data used in the RSM method were complemented with more samples. It should be remarked that, although DoE ensures data well distributed throughout all the input data range, the ANN model, which is exclusively data-based, can present abrupt nonlinearities in the responses if the amount of data is not large enough, and if the data set is not well distributed. This fact can be especially significant when the range of the input data is large, and some of these parameters have a clear nonlinear influence on the responses, as is the case of feed water salt concentration in this study. Thus, Appendix A shows all the experimental data. Besides, it should be commented that, as in the case of experimental data used in RSM model, four measurements were taken for each experimental point.

The experimental data set was divided in 3 subsets: i) training subset (75% of samples), ii) validation subset (20% of samples), and iii) test subset (5% of samples). Moreover, in order to avoid overfitting during the training process, both the input and output variables were normalized in the range 0.1-0.9 by means of the following expression [10]:

$$y_n = (1 - U - L) \cdot \frac{y_k - y_{min}}{y_{max} - y_{min}} + L, \tag{11}$$

where y_n is the normalized sample, y_k is the actual sample, y_{max} and y_{min} are the maximum and minimum value of the variable to be normalized, and U and L are the upper and lower bounds considered to define the output network range ($U = L = 0.1$).

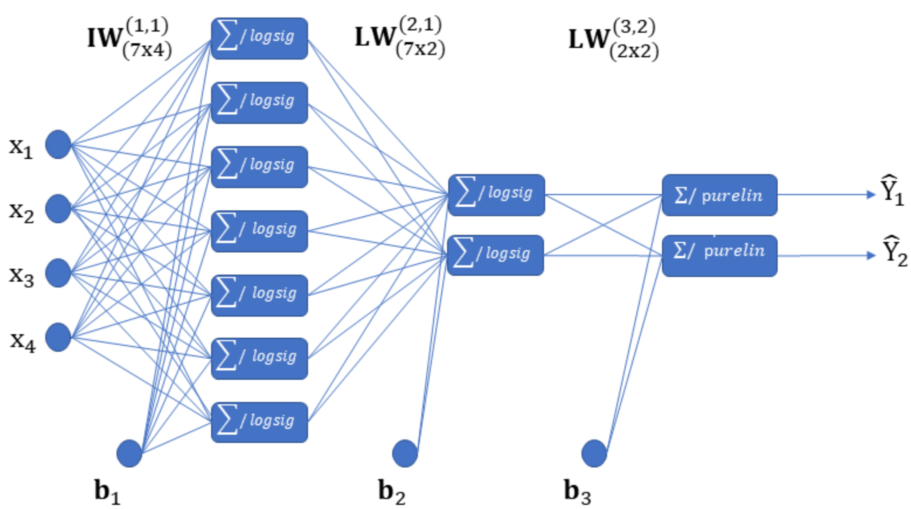

Figure 5: Schematic diagram of the optimal network architecture. x_1, x_2, x_3 and x_4 are S, T_{cond}, T_{evap} and F, while $\hat{Y}_1$ and $\hat{Y}_2$ are P_{flux} and STEC.

The training process was accomplished in the Neural Network Toolbox of MATLAB, using the Lavenberg-Marquardt BP algorithm [40]. Several ANN architectures were tested varying the number of hidden layers between 1-3 and the number of neurons in each layer between 1-10. The transfer function adopted in the hidden layers was the *logsig*, whereas the one employed in the output layer was the *purelin*. The optimal architecture was selected according to the performance function (RMSE).

Input weight matrix	$\mathbf{IW}^{(1,1)} =$	$\begin{vmatrix} -1.441 & 0.890 & 0.372 & -2.015 \\ -1.528 & 1.047 & 0.516 & -2.105 \\ -0.831 & -0.541 & 0.926 & 0.213 \\ 2.115 & 1.427 & 0.796 & 0.612 \\ -1.957 & 0.117 & 0.139 & -0.472 \\ 0.023 & -0.053 & 0.177 & 0.210 \\ -0.698 & 0.842 & 1.351 & -0.953 \end{vmatrix}$
Hidden layer 1 bias vector	$\mathbf{b}_{(1)} =$	$\begin{vmatrix} 2.148 \\ 2.269 \\ 2.840 \\ -0.788 \\ -1.478 \\ -0.042 \\ -4.384 \end{vmatrix}$
Hidden layer 2 weight matrix	$\mathbf{LW}^{(2,1)\mathrm{T}} =$	$\begin{vmatrix} -0.610 & -0.593 \\ 0.450 & 0.461 \\ -1.086 & -0.257 \\ -0.011 & 0.049 \\ -0.593 & -0.408 \\ -0.974 & -1.613 \\ -0.280 & 0.467 \end{vmatrix}$
Hidden layer 2 bias vector	$\mathbf{b}_{(2)} =$	$\begin{vmatrix} -0.680 \\ 1.162 \end{vmatrix}$
Output layer weight matrix	$\mathbf{LW}^{(3,2)}$	$\begin{vmatrix} 1.860 & -0.030 \\ -0.094 & -1.518 \end{vmatrix}$
Output layer bias vector	$\mathbf{b}_{(3)} =$	$\begin{vmatrix} 0.844 \\ 0.398 \end{vmatrix}$

Table 6: Optimal network weights and bias.

The optimal ANN model (see Fig. 5) is composed by 4 inputs, two hidden layers containing 7 and 2 neurons respectively, and two outputs. This feedforward neural network topology can be described as MLP (4:7:2:2). Notice that the training process was iteratively performed (as was metioned in Section 2.4) until reaching a RMSE sufficiently small, according to the imposed goal for the training subset (RMSE$\leq 5\cdot 10^{-4}$, normalized value according to Eq. 11). In the optimal network case, the training process was stopped after 13 iterations obtaining a RMSE$=2.61\cdot 10^{-4}$ for the training data subset, while the RMSE of the validation and test subsets was lower than $1\cdot 10^{-3}$. Tab. 6 summarizes the optimal values of network weights and bias in a matrix-vector format. The ANN model can be expressed as:

$$\hat{\mathrm{Y}} = \Phi^{(3)}(\mathbf{LW}^{(3,2)}\Phi^{(2)}(\mathbf{LW}^{(2,1)}\Phi^{(1)}(\mathbf{IW}^{(1,1)}\mathbf{x} + \mathbf{b}^{(1)}) + \mathbf{b}^{(2)}) + \mathbf{b}^{(3)}), \quad (12)$$

where $\Phi^{(i)}$ is the transfer function correspondent to layer i (i=1-3), $\mathbf{LW}^{(2,1)}$ and $\mathbf{LW}^{(3,2)}$ are the layer weight matrices, where the superscripts indicates the destination and source connections, $\mathbf{IW}^{(1,1)}$ is the input weight matrix, $\mathbf{x}$ is the network input, and $\hat{\mathrm{Y}}$ is the network output. It should be commented that the same notation has been employed in Tab. 6 and Fig. 5.

The fit between the experimental data used in the training and validation processes, and the predicted values by the ANN model are shown in Fig. 6. Besides, Tab. 7 shows the analysis of variance (ANOVA) for these two subsets. As can be observed, the obtained p-values (lower than 0.05) and coefficients of determination (close to 1) evidence the good fit obtained by ANN model in both cases P_{flux} and STEC. Notice that in the next subsection more experimental data will be used to test the performance of the ANN model.

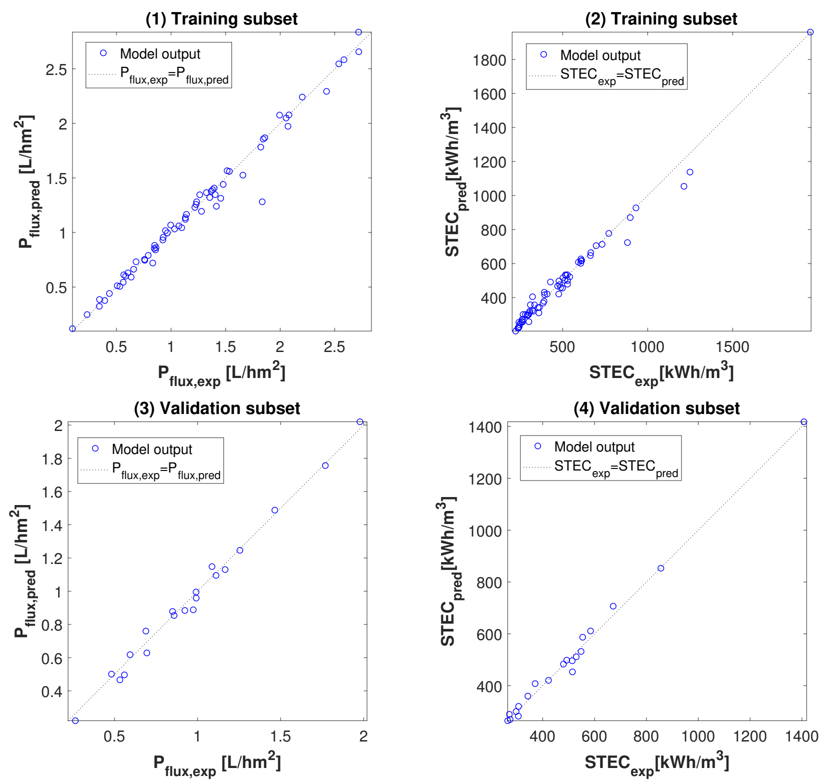

Figure 6: Comparison between predicted values by ANN model ($\mathrm{STEC_{pred}}$ and $\mathrm{P_{flux,pred}}$) and experimental data ($\mathrm{STEC_{exp}}$ and $\mathrm{P_{flux,exp}}$).

	P_{flux}		STEC	
	Training	Validation	Training	Validation
p-value	≤0.01	≤0.01	≤0.01	≤0.01
R^2	0.994	0.991	0.993	0.990
adjusted-R^2	0.993	0.990	0.992	0.989

Table 7: Goodness of the adjustment of ANN model.

3.3. Comparison between the prediction abilities of the two modeling approaches.

In order to compare in the same conditions the prediction abilities of the RSM and ANN models, additional experimental data were employed (see Tab. 8). The comparison were performed based on the Root Mean Square Error (RMSE), the coefficient of determination (R^2) and the adjusted-R^2.

S (g/L)	T_{cond}(°C)	T_{evap}(°C)	F(L/h)	STEC(kWh/m^3)	P_{flux}(L/(h·m^3))
35	20	75	600	297.563	2.303
35	25	75	400	246.323	1.568
35	30	65	500	286.500	1.311
60	20	65	600	506.388	1.141
60	25	65	500	535.293	0.756
60	30	65	400	453.794	0.580
60	30	75	600	368.303	1.524
140	20	75	500	499.528	1.054
140	25	65	600	678.193	0.736
140	30	65	400	1172.35	0.214

Table 8: Additional experimental data used to compare the two modeling approaches.

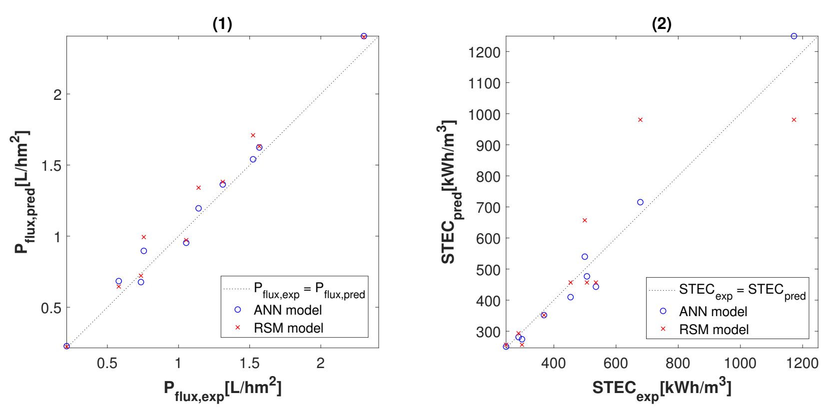

Figure 7: Comparison between predicted values of both models ($STEC_{pred}$ and $P_{flux,pred}$) and experimental data ($STEC_{exp}$ and $P_{flux,exp}$).

	RSM		ANN	
	STEC	P_{flux}	STEC	P_{flux}
RMSE	85.70	0.10	27.01	0.06
R^2	0.770	0.985	0.982	0.988
adjusted-R^2	0.742	0.984	0.981	0.987

Table 9: Comparison of predictive abilities of RSM and ANN.

Fig. 7 shows the correlation between the additional experimental data and the predicted values, and Tab. 9 shows the performance metrics. On the one hand, in the case of the permeate flux (P_{flux}), the R^2 and the adjusted-R^2 values obtained with both models were similar (very close to 1, see Fig. 7), whereas the obtained RMSE error was 0.06 and 0.10 ($L/(h{\cdot}m^2)$) for the ANN and RSM model respectively, which evidences the good results obtained with both models. On the other hand, in the STEC case, the R^2 and the adjusted-R^2 values obtained with the ANN model were 0.982 and 0.981 respectively, whereas the ones obtained with the RSM model were 0.770 and 0.742 respectively. The RMSE of the ANN model was 27.01 (kWh/m^3) while the RMSE of the RSM model was 85.70 (kWh/m^3). It should be taken into account that the low grade of adjustment obtained by the RSM model in the STEC case can be explained for two main reasons: (1) the nonlinear behaviour of STEC with respect to feed water salt concentration, and (2) the simplified equation modeling STEC does not consider the influence of T_{cond} and F in the responses, hence it adds uncertainty to the model (see Eq. 10). Thus, it can be concluded that the ANN model is more suitable for predicting STEC, specially when working at high feed water salt concentration.

In addition to the comparison carried out previously, 3D response surfaces were displayed to observe the influence of the feed water salt concentration in both P_{flux} and STEC, and also to compare the surfaces provided by RSM and ANN models. It should be taken into account that the influence of the rest of input variables was studied in [12]. Thus, Figs. 8 and 9 show the 3D response surfaces for RSM and ANN models respectively.

On one hand, it can be observed in Fig. 8-1, 3 and 5, and in Fig. 9-1, 3 and 5 the influence of the feed water salt concentration and the other input variables (T_{evap}, T_{cond} and F) in the P_{flux} predicted by the RSM and ANN models respectively. It can been seen that P_{flux} decreases significantly with increasing feed water salt concentration. Notice that, the 3D response surfaces obtained by the two models were similar, due to P_{flux} being almost linear in all the input data range.

On the other hand, in Fig. 8-2, 4 and 6, and in Fig. 9-2, 4 and 6 the effects of S, T_{evap}, T_{cond} and F on the STEC predicted by the RSM and ANN models are shown. In this case, the opposite behaviour than in P_{flux} can be observed, STEC augments when increasing feed water salt concentration. Therefore, an increase in the salinity implies a decrease in thermal efficiency. Besides, some differences can be seen in the 3D response surfaces of both models. RSM model provides almost linear surfaces for the whole input data range, whereas ANN model provides nonlinear surfaces which represent in a more accurate way the behaviour of STEC observed from experimental data (see Appendix A). In addition, ANN model takes into consideration the influence of T_{cond} and F in the response (see Fig. 9-4 and 6), whereas RSM model does not consider these variables (see Eq. 10) as was commented before.

According to the results obtained, different interaction effects can be seen among the input variables. Considering T_{evap} and S, the increase of T_{evap} yields to an increase of the performance, namely, an increase of P_{flux} and a decrease of STEC, and this effect is stronger the higher the S values. The increase of S leads to a decrease of the performance and this effect is stronger for smaller T_{evap}. Regarding the interaction effect between F and S, an increase of F at different S values causes an enhancement of P_{flux}. However, the effect of increasing F on STEC depends on S. For a salinity value of 35 g/L, an increase of F causes a negative effect on STEC, while for high S values, an increase of F produces the contrary effect. This is because at high S and low F, the permeate production decreases at a higher rate than the decrease of the external heat necessary by working with a low F. Finally, the effect of T_{cond} on the P_{flux} is negative. An increase of this variable, yields to a decrease of the driving force, diminishing P_{flux} and this effect is stronger for high S. Regarding the STEC, at a salinity of 35 g/L, an increase of T_{cond} favours the decline of the STEC, however, at high S values, the increase of T_{cond} leads to an increase of STEC because the decrease of P_{flux} at high S is more pronounced.

From an optimization point of view, two interesting conclusions can be drawn. Firstly, in Fig. 9-6 it can be observed how STEC decreases at low F when S is in a low-medium range, and then, at high S, STEC has an almost curvilinear behaviour with respect F where the minimum value is located around 500 L/h. Secondly, it can be observed that the STEC does not present large variations with respect to T_{evap} at low S, around 80 kWh/m^3 at 500 L/h (see Fig. 9-1). However, at high salinity concentrations (i.e. 140 g/L), the influence is remarkable, around 500 kWh/m^3 at 500 L/h (see Fig. 9-1). This fact can be very relevant in solar powered batch operations since the result of an optimization problem with a time horizon of one day could be: working at low T_{evap} at low salinity concentrations and storing thermal energy to be able to operate at high temperature, significantly improving performance, when high salinity ranges are reached.

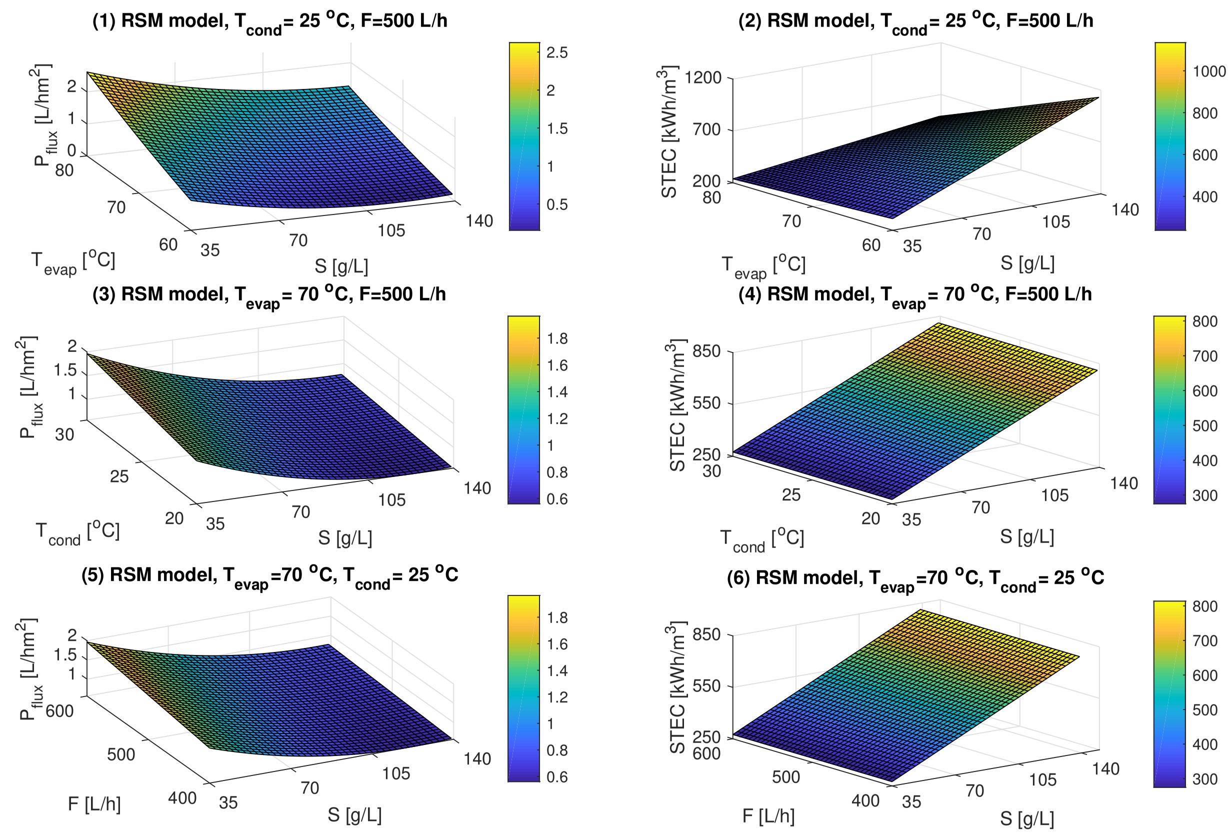

Figure 8: 3D response surfaces obtained by RSM model.

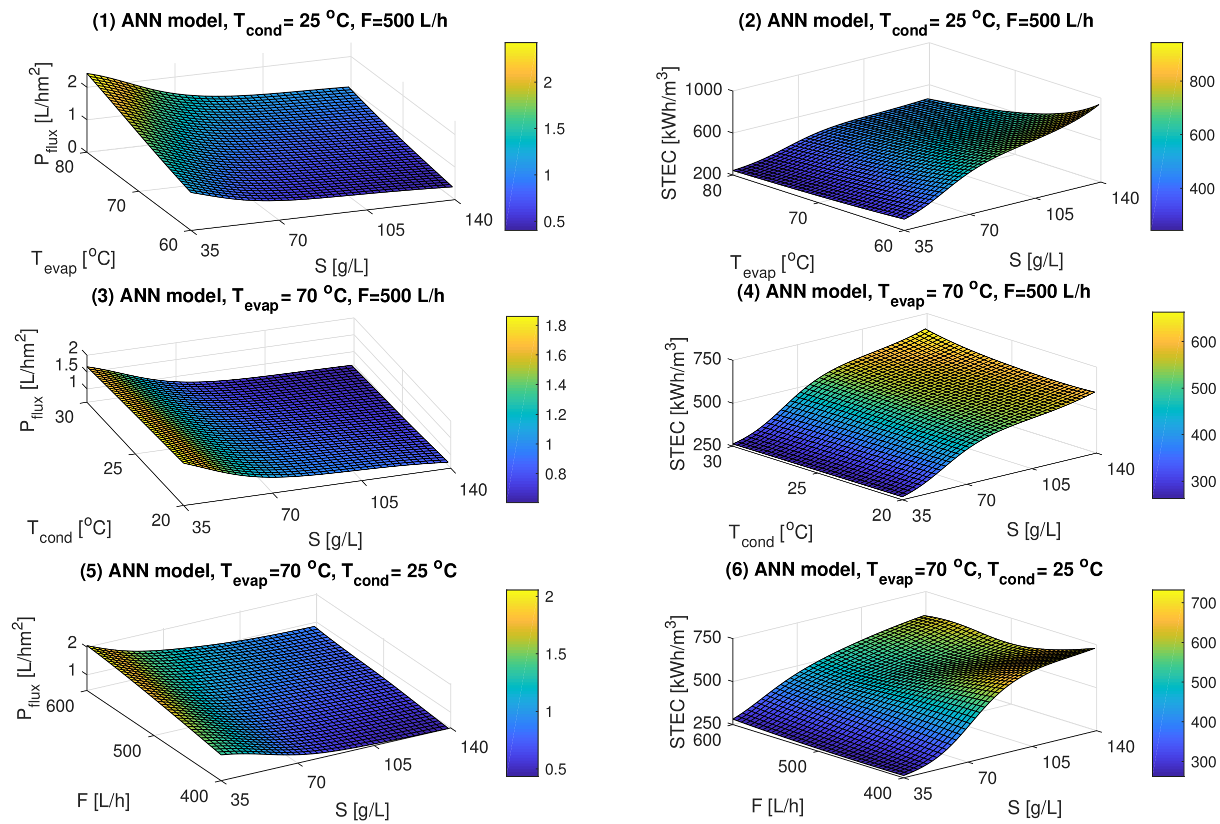

Figure 9: 3D response surfaces obtained by ANN model.

3.4. Multi-objective optimization

Once the models were developed, validated and compared, a multi-objective optimization was carried out using NSGA-II algorithm. The objective was to find a set of solutions that ensure a trade-off between the two performance parameters (maximizing P_{flux} and minimizing STEC), that require contrary operating conditions in some variables such as T_{cond} and F. This set of optimal solution is known as *Pareto Front* or *nondominant solutions*. Thus, two optimization cases were proposed according to the levels of feed water salt concentration that can be reached when performing batch operation for desalting RO brines. In the first optimization problem, the feed water salt concentration was fixed at 70 g/L, whereas in the second optimization problem, the feed water salt concentration was fixed at 105 g/L. Notice that the optimized variables in both cases are T_{cond}, T_{evap}, and F, since they can be easily manipulated to achieve the desired performance. The optimization was carried out using only the ANN model as it takes into account all the input variables for the two performance parameters, as was commented in the previous section. The results obtained for both optimization cases are reported in Fig. 10 and Tab. 10. In addition, three experimental runs randomly selected were performed in order to validate the optimal points obtained in the two optimization problems (see Tab. 11).

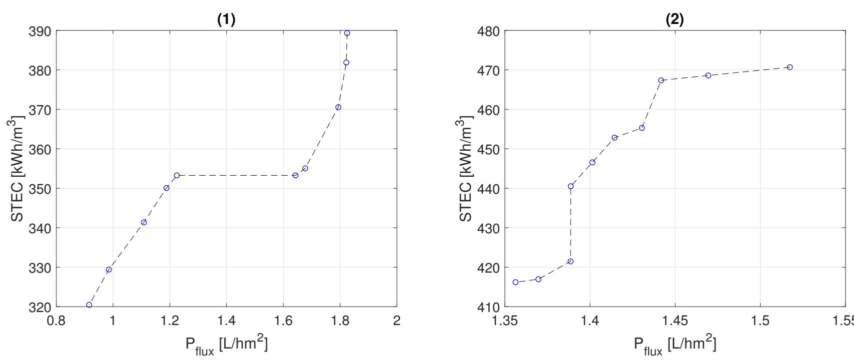

Figure 10: Pareto fronts of the two optimization cases. (1) Results related to optimization problem 1, and (2) results related to optimization problem 2.

Attending to the results, Tab. 10 shows that different operating conditions are required in some of the parameters depending on the level of feed water salinity. Notice that the pareto fronts must be analyzed by assigning different importance for responses, according to the specific desirability of the application. In general, it can be seen that in the two studied cases, for applications that require higher distillate production it is better to operate with larger F and smaller T_{cond}. However, if the thermal efficiency is the decisive factor in the application, it is better to operate with smaller F and larger T_{cond} at the feed water salinity of 70 g/L. On the other hand, at the feed water salinity of 105 g/L, larger T_{cond} and larger F are required. It is also important to remark that in the

Run	T_{cond}(°C)	T_{evap}(°C)	F(L/h)	$STEC_{pred}$ (kWh/m^3)	$P_{flux,pred}$ (L/(h·m^2))
Pareto front values of optimization problem 1					
1	20.00	80.00	600.00	389.31	1.83
2	20.31	80.00	577.04	381.85	1.82
3	21.09	80.00	557.45	370.53	1.79
4	28.81	80.00	599.86	355.03	1.67
5	30.00	80.00	597.49	353.26	1.64
6	26.64	80.00	436.35	353.26	1.22
7	26.84	80.00	426.97	350.05	1.18
8	26.85	80.00	401.38	341.36	1.10
9	29.67	80.00	412.29	329.42	0.98
10	30.00	80.00	400.00	320.47	0.91
Pareto front values of optimization problem 2					
1	20.00	80.00	600.00	470.67	1.51
2	21.02	80.00	598.73	468.58	1.46
3	21.49	80.00	595.28	467.35	1.44
4	20.62	80.00	556.64	455.28	1.43
5	21.11	80.00	557.07	452.81	1.41
6	21.40	80.00	548.95	446.56	1.40
7	21.33	80.00	532.78	440.51	1.38
8	30.00	80.00	600.00	421.48	1.38
9	29.86	80.00	585.48	416.96	1.36
10	30.00	80.00	580.10	416.20	1.35

Table 10: Values of the Pareto fronts obtained by ANN model for both optimization problems.

Run in the optimization	$STEC_{pred}$ (kWh/m^3)	$P_{flux,pred}$ (L/(h·m^2))	$STEC_{exp}$ (kWh/m^3)	$P_{flux,exp}$ (L/(h·m^2))
Confirmation runs of optimization problem 1				
3	370.53	1.79	361.50	1.79
6	353.26	1.22	360.10	1.18
8	341.36	1.10	357.15	1.02
Confirmation runs of optimization problem 2				
1	470.67	1.51	474.97	1.48
4	455.28	1.43	456.08	1.46
5	452.81	1.41	454.38	1.40

Table 11: Validation of the optimal operating points.

two optimization problems, the inlet evaporator channel temperature is at the maximum (80 °C) for all the pareto solutions. Nevertheless, in real solar powered operations, this temperature will be limited by the irradiance conditions at every moment and, therefore, the optimal operating conditions can be obtained by modifying only T_{cond} and F. It should be pointed out that T_{cond} steadily increases when performing batch operations, but it could be manipulated using cooling devices in order to work in the optimal operating points, thus increasing MD module performance.

Moreover, Tab. 12 shows the salt rejection factor (SRF) for each of the studied salinities. For the three salinities, the SRF was close to 100 %, confirming that in this case, in accordance with the MD fundamentals, the operating conditions do not affect the salinity of permeate [44].

S (g/L)	T_{cond}(°C)	T_{evap}(°C)	F(L/h)	SRF (%)
35	20.00	80.00	583.00	99.99 %
70	21.10	80.00	558.00	99.99 %
105	20.60	80.00	557.45	99.99 %

Table 12: Salt rejection factor for each salinity.

4. Conclusion

Response Surface Methodology (RSM) and Artificial Neural Networks (ANN) were used for modeling the performance of a commercial-scale PGMD module, under the operating conditions required by one of its possible potential industrial implementation: desalting brines from RO plants. The independent variables chosen for the models were the condenser inlet temperature (20-30 °C), the evaporator inlet temperature (60-80 °C), the feed flow rate (400-600 L/h) and the feed water salt concentration (35-140 g/L), while permeate flux (L/(h·m^2)) and Specific Thermal Energy Consumption (STEC, kWh/m^3) were selected as predicted variables. The prediction abilities of the two modeling tools were compared with further experimental data. In addition, the optimal operating conditions (maximizing and minimizing P_{flux} and STEC respectively) for two of the feed salinity concentrations (70 and 105 g/L) that can be reached when performing batch operation for desalting RO brines were determined.

Regarding the models, the ANN model achieved higher accuracy in predicting the responses, specially in the STEC case. This fact can be explained since the feed water salt concentration affects the STEC on a nonlinear way, which cannot be well represented by a quadratic equation. Therefore, ANN model is shown to be more adequate than RSM for developing models in which the feed water salt concentration is considered as an input. However, it should be also commented that it required more experimental data.

The multi-objetive optimization carried out revealed that, depending of the level of feed water salinity, different operating conditions are required in some of the parameters. Therefore, real time multi-objective optimization could be essential for performing batch operations aimed at desalting RO brines, specially when the MD facility is powered by solar energy.

In future works, the models presented in this paper will be used for developing optimization algorithms able to perform optimal designs of a solar powered MD facility to be integrated in a RO plant. In the same way, models will be used for optimizing the solar powered operation of the MD module in batch mode operation.

Acknowledgments

This work has been funded by the National R+D+i Plan Projects DPI2014-56364-C2-1/2-R and DPI2017-85007-R of the Spanish Ministry of Economy, Industry and Competitiveness and ERDF funds.

Appendix A. Experimental data

Run	ANN subset	Used in RSM	S (g/L)	T_{cond}(°C)	T_{evap}(°C)	F(L/h)	STEC(kWh/m^3)	P_{flux}(L/(h·m^2))
1	Validation	Yes	35	20	60	400	300.305	0.995
2	Training	No	35	20	70	400	369.411	1.440
3	Training	Yes	35	20	80	400	222.526	1.973
4	Training	No	35	20	60	500	356.991	1.257
5	Training	No	35	20	70	500	300.350	1.867
6	Training	No	35	20	80	500	229.492	2.545
7	Validation	Yes	35	20	60	600	359.706	1.487
8	Training	No	35	20	70	600	298.275	2.077
9	Training	Yes	35	20	80	600	260.154	2.656
10	Training	No	35	25	60	400	298.676	0.954
11	Training	No	35	25	70	400	255.285	1.378
12	Training	No	35	25	80	400	222.468	1.856
13	Validation	No	35	25	60	500	320.154	1.130
14	Validation	Yes	35	25	70	500	264.936	1.756
15	Training	No	35	25	80	500	254.171	2.293
16	Training	No	35	25	60	600	356.744	1.391
17	Training	No	35	25	70	600	300.857	2.048
18	Training	No	35	25	80	600	250.845	2.306
19	Validation	Yes	35	30	60	400	282.328	0.854
20	Training	No	35	30	70	400	271.258	1.281
21	Training	Yes	35	30	80	400	202.907	1.320
22	Training	No	35	30	60	500	319.819	1.043
23	Training	No	35	30	70	500	271.653	1.525
24	Training	No	35	30	80	500	219.481	2.241

The table continues in the next page

Run	ANN subset	Used in RSM	S (g/L)	T_{cond}(°C)	T_{evap}(°C)	F(L/h)	STEC(kWh/m^3)	P_{flux}(L/(h·m^2))
25	Training	Yes	35	30	60	600	319.630	1.365
26	Validation	No	35	30	70	600	269.584	2.019
27	Training	Yes	35	30	80	600	240.578	2.583
28	Validation	No	60	20	60	400	483.201	0.618
29	Validation	No	60	20	70	400	407.835	0.888
30	Training	No	60	20	80	400	257.824	1.560
31	Training	No	60	20	60	500	515.713	0.745
32	Training	No	60	20	70	500	416.734	1.230
33	Training	No	60	20	80	500	404.528	1.281
34	Training	No	60	20	60	600	521.765	1.016
35	Training	No	60	20	70	600	491.363	1.313
36	Training	No	60	20	80	600	309.722	2.076
37	Training	No	60	25	60	400	420.777	0.612
38	Training	No	60	25	70	400	342.163	0.931
39	Training	No	60	25	80	400	294.926	1.240
40	Test	No	60	25	60	500	545.728	0.654
41	Training	No	60	25	70	500	378.013	1.166
42	Test	No	60	25	80	500	305.985	1.620
43	Validation	No	60	25	60	600	453.292	0.884
44	Training	No	60	25	70	600	420.574	1.347
45	Test	No	60	25	80	600	334.478	1.978
46	Validation	No	60	30	60	400	498.438	0.466
47	Training	No	60	30	70	400	340.396	0.840
48	Validation	No	60	30	80	400	289.640	1.095
49	Training	No	60	30	60	500	533.780	0.591
50	Training	Yes	60	30	70	500	367.792	1.032
51	Training	No	60	30	80	500	310.756	1.566

The table continues in the next page

Run	ANN subset	Used in RSM	S (g/L)	T_{cond}(°C)	T_{evap}(°C)	F(L/h)	STEC(kWh/m^3)	P_{flux}(L/(h·m^2))
52	Training	No	60	30	60	600	529.871	0.720
53	Training	No	60	30	70	600	430.971	1.194
54	Training	No	60	30	80	600	325.401	1.782
55	Training	Yes	87.5	25	60	500	705.05	0.506
56	Training	Yes	87.5	20	70	500	501.44	0.996
57	Training	Yes	87.5	25	70	400	615.29	0.544
58	Training	Yes	87.5	25	70	500	500.06	0.882
59	Training	Yes	87.5	25	70	600	496.07	1.148
60	Training	Yes	87.5	30	70	500	532.01	0.760
61	Training	Yes	87.5	25	80	500	420.44	1.246
62	Training	Yes	140	20	60	400	927.252	0.324
63	Validation	No	140	20	70	400	706.733	0.496
64	Training	Yes	140	20	80	400	478.825	0.853
65	Validation	No	140	20	60	500	853.079	0.501
66	Training	No	140	20	70	500	626.960	0.790
67	Training	No	140	20	80	500	459.124	1.120
68	Training	Yes	140	20	60	600	777.253	0.663
69	Validation	No	140	20	70	600	611.118	0.958
70	Training	Yes	140	20	80	600	475.667	1.407
71	Training	No	140	25	60	400	1137.747	0.147
72	Training	No	140	25	70	400	713.008	0.441
73	Validation	No	140	25	80	400	586.875	0.628
74	Test	No	140	25	60	500	960.347	0.396
75	Training	Yes	140	25	70	500	601.207	0.732
76	Training	No	140	25	80	500	467.379	1.060
76	Training	No	140	25	60	600	870.252	0.511
78	Training	No	140	25	70	600	618.107	0.861

The table continues in the next page

Run	ANN subset	Used in RSM	S (g/L)	T_{cond}(°C)	T_{evap}(°C)	F(L/h)	STEC(kWh/m^3)	P_{flux}(L/(h·m^2))
79	Training	No	140	25	80	600	455.628	1.345
80	Training	Yes	140	30	60	400	1960.897	0.118
81	Training	No	140	30	70	400	723.315	0.385
82	Training	Yes	140	30	80	400	607.823	0.600
83	Validation	No	140	30	60	500	1418.157	0.220
84	Training	No	140	30	70	500	647.301	0.630
85	Training	No	140	30	80	500	497.021	1.068
86	Training	Yes	140	30	60	600	1054.110	0.376
87	Training	No	140	30	70	600	663.802	0.753
88	Training	Yes	140	30	80	600	533.632	1.135

Table 13: Experimental data used for RSM and ANN modeling

References

[1] J. P. Mericq, S. Laborie, C. Cabassud, Vacuum membrane distillation of seawater reverse osmosis brines, Water Research 44 (2010) 5260–5273.

[2] D. Qu, J. Wang, B. Fan, Z. Luan, D. Hou, Study on concentrating primary reverse osmosis retentate by direct contact membrane distillation, Desalination 247 (2009) 540–550.

[3] C. R. Martinetti, A. E. Childress, T. Y. Cath, High recovery of concentrated RO brines using forward osmosis and membrane distillation, Journal of membrane science 331 (2009) 31–39.

[4] J. Sanmartino, M. Khayet, M. García-Payo, H. El-Bakouri, A. Riaza, Treatment of reverse osmosis brine by direct contact membrane distillation: Chemical pretreatment approach, Desalination 420 (2017) 79–90.

[5] A. Alkhudhiri, N. Darwish, N. Hilal, Membrane distillation: a comprehensive review, Desalination 287 (2012) 2–18.

[6] M. Khayet, Solar desalination by membrane distillation: Dispersion in energy consumption analysis and water production costs (a review), Desalination 308 (2013) 89–101.

[7] E. Drioli, A. Ali, F. Macedonio, Membrane distillation: Recent developments and perspectives, Desalination 356 (2015) 56–84.

[8] N. Thomas, M. O. Mavukkandy, S. Loutatidou, H. A. Arafat, Membrane distillation research & implementation: Lessons from the past five decades, Separation and Purification Technology 189 (2017) 108–127.

[9] M. Khayet, C. Cojocaru, A. Baroudi, Modeling and optimization of sweeping gas membrane distillation, Desalination 287 (2012) 159–166.

[10] M. Khayet, C. Cojocaru, Artificial neural network modeling and optimization of desalination by air gap membrane distillation, Separation and Purification Technology 86 (2012) 171–182.

[11] M. Khayet, C. Cojocaru, Artificial neural network model for desalination by sweeping gas membrane distillation, Desalination 308 (2013) 102–110.

[12] A. Ruiz-Aguirre, J. Andrés-Mañas, J. Fernández-Sevilla, G. Zaragoza, Modeling and optimization of a commercial permeate gap spiral wound membrane distillation module for seawater desalination, Desalination 419 (2017) 160–168.

[13] J. D. Gil, L. Roca, A. Ruiz-Aguirre, G. Zaragoza, M. Berenguel, Optimal operation of a solar membrane distillation pilot plant via nonlinear model predictive control, Computers & Chemical Engineering 109 (2018) 151–165.

[14] R. Porrazzo, A. Cipollina, M. Galluzzo, G. Micale, A neural network-based optimizing control system for a seawater-desalination solar-powered membrane distillation unit, Computers & Chemical Engineering 54 (2013) 79–96.

[15] Y.-H. Chen, Y.-W. Li, H. Chang, Optimal design and control of solar driven air gap membrane distillation desalination systems, Applied Energy 100 (2012) 193–204.

[16] I. Hitsov, T. Maere, K. De Sitter, C. Dotremont, I. Nopens, Modelling approaches in membrane distillation: a critical review, Separation and Purification Technology 142 (2015) 48–64.

[17] M. Khayet, C. Cojocaru, M. Essalhi, Artificial neural network modeling and response surface methodology of desalination by reverse osmosis, Journal of Membrane Science 368 (2011) 202–214.

[18] A. E. Khalifa, D. U. Lawal, Application of response surface and Taguchi optimization techniques to air gap membrane distillation for water desalination: A comparative study, Desalination and Water Treatment 57 (2016) 28513–28530.

[19] S. T. Bouguecha, A. Boubakri, S. E. Aly, M. H. Al-Beirutty, M. M. Hamdi, Optimization of permeate flux produced by solar energy driven membrane distillation process using central composite design approach, Water Science and Technology 74 (2016) 87–98.

[20] T. Mohammadi, P. Kazemi, M. Peydayesh, Optimization of vacuum membrane distillation parameters for water desalination using Box–Behnken design, Desalination and Water Treatment 56 (2015) 2306–2315.

[21] A. Boubakri, A. Hafiane, S. A. T. Bouguecha, Application of response surface methodology for modeling and optimization of membrane distillation desalination process, Journal of Industrial & Engineering Chemistry 20 (2014) 3163–3169.

[22] M. Khayet, C. Cojocaru, Air gap membrane distillation: Desalination, modeling and optimization, Desalination 287 (2012) 138–145.

[23] H. Chang, J.-S. Liau, C.-D. Ho, W.-H. Wang, Simulation of membrane distillation modules for desalination by developing user's model on Aspen Plus platform, Desalination 249 (2009) 380–387.

[24] M. Khayet, C. Cojocaru, C. García-Payo, Application of response surface methodology and experimental design in direct contact membrane distillation, Industrial & Engineering Chemistry Research 46 (2007) 5673–5685.

[25] D. Cheng, W. Gong, N. Li, Response surface modeling and optimization of direct contact membrane distillation for water desalination, Desalination 394 (2016) 108–122.

[26] Q. He, P. Li, H. Geng, C. Zhang, J. Wang, H. Chang, Modeling and optimization of air gap membrane distillation system for desalination, Desalination 354 (2014) 68–75.

[27] W. Cao, Q. Liu, Y. Wang, I. M. Mujtaba, Modeling and simulation of VMD desalination process by ANN, Computers & Chemical Engineering 84 (2016) 96–103.

[28] M. Tavakolmoghadam, M. Safavi, An optimized neural network model of desalination by vacuum membrane distillation using genetic algorithm, Procedia Engineering 42 (2012) 106–112.

[29] S. Shirazian, M. Alibabaei, Using neural networks coupled with particle swarm optimization technique for mathematical modeling of air gap membrane distillation (AGMD) systems for desalination process, Neural Computing and Applications 28 (2017) 2099–2104.

[30] D. Cheng, N. Li, J. Zhang, Modeling and multi-objective optimization of vacuum membrane distillation for enhancement of water productivity and thermal efficiency in desalination, Chemical Engineering Research and Design 132 (2018) 697–713.

[31] Y. Zhou, M. Huang, Q. Deng, T. Cai, Combination and performance of forward osmosis and membrane distillation (FO-MD) for treatment of high salinity landfill leachate, Desalination 420 (2017) 99–105.

[32] N. U. Kumar, A. Martin, Experimental modeling of an air-gap membrane distillation module and simulation of a solar thermal integrated system for water purification, Desalination and Water Treatment 84 (2017) 123–134.

[33] J. D. Gil, L. Roca, G. Zaragoza, M. Berenguel, A feedback control system with reference governor for a solar membrane distillation pilot facility, Renewable Energy 120 (2018) 536–549.

[34] H. C. Duong, P. Cooper, B. Nelemans, T. Y. Cath, L. D. Nghiem, Evaluating energy consumption of air gap membrane distillation for seawater desalination at pilot scale level, Separation and Purification Technology 166 (2016) 55–62.

[35] E. Guillén-Burrieza, G. Zaragoza, S. Miralles-Cuevas, J. Blanco, Experimental evaluation of two pilot-scale membrane distillation modules used for solar desalination, Journal of Membrane Science 409 (2012) 264–275.

[36] G. Zaragoza, A. Ruiz-Aguirre, E. Guillén-Burrieza, Efficiency in the use of solar thermal energy of small membrane desalination systems for decentralized water production, Applied Energy 130 (2014) 491–499.

[37] W. J. Hill, W. G. Hunter, A review of response surface methodology: a literature survey, Technometrics 8 (1966) 571–590.

[38] G. E. Box, K. B. Wilson, On the experimental attainment of optimum conditions, in: Breakthroughs in Statistics, Springer, 1992, pp. 270–310.

[39] L. Stahle, S. Wold, et al., Analysis of variance (ANOVA), Chemometrics and Intelligent Laboratory Systems 6 (1989) 259–272.

[40] M. H. Beale, M. T. Hagan, H. B. Demuth, Neural Network Toolbox: User's Guide (Version 10.0), 2017.

[41] M. T. Hagan, H. B. Demuth, Neural networks for control, in: American Control Conference, 1999. Proceedings of the 1999, volume 3, IEEE, 1999, pp. 1642–1656.

[42] H. B. Demuth, M. H. Beale, O. De Jess, M. T. Hagan, Neural network design, PWS Publishing Co., 2014.

[43] K. Deb, A. Pratap, S. Agarwal, T. Meyarivan, A fast and elitist multiobjective genetic algorithm: NSGA-II, IEEE Transactions on Evolutionary Computation 6 (2002) 182–197.

[44] D. Winter, J. Koschikowski, M. Wieghaus, Desalination using membrane distillation: Experimental studies on full scale spiral wound modules, Journal of Membrane Science 375 (2011) 104–112.